**Journal of the European Optical
Society-Rapid Publications**

**RESEARCH ARTICLE**                                                **OPEN  ACCESS**

# Brillouin scattering spectroscopy for studying human anatomy: Towards *in situ* mechanical characterization of soft tissue

Paata Pruidze[1,2], Elena Chayleva[3], Wolfgang J. Weninger[1,2], and Kareem Elsayad[1,2,*]

[1] Division of Anatomy, Center for Anatomy and Cell Biology, Medical University of Vienna, 1090 Vienna, Austria
[2] Medical Imaging Cluster (MIC), Medical University of Vienna, 1090 Vienna, Austria
[3] Max Perutz Laboratories, University of Vienna, 1030 Vienna, Austria

**Abstract.** Brillouin light scattering (BLS) spectroscopy is a label-free method of measuring the GHz-frequency viscoelastic properties. The measured longitudinal modulus is acutely sensitive to the degree of hydration, crosslinking, and temperature, which can be indicative of tissue health. As such, performing *in situ* measurements on humans is particularly desirable for exploring potential clinical translation, however, is not possible with existing designs which are coupled to bench-top microscopes. Here we introduce a robust fiber coupled hand-held BLS probe and demonstrate its reliability for measuring excised human tissue. We verify its accuracy using confocal BLS microscopy and further show that it is possible to distinguish veins, arteries, nerves and muscles based on their BLS-measured viscoelasticity. This provides a necessary first step towards *in situ* clinical BLS viscoelasticity studies of human tissue.

## 1 Introduction

Mechanical properties play an essential role in the physiological processes of soft tissue, with the onset of many diseases associated with changes therein [1]. They can also serve as a direct measure of tissue health [2], and anomalies may be indicative of pathologies beyond those of the probed tissue [3]. There are numerous metrics for assessing the mechanical properties, with often disparate results and interpretations of the measured parameters [4, 5]. While the discrepancies in some cases result from the different measurement techniques and methodologies used, they are pervasive also when this is not the case, and often tied to the practical challenges of performing measurements in a minimally invasive/ perturbative manner. Despite much progress in recent years, significant challenges remain for quantitative diagnostics based on changes in the mechanical properties of soft tissue [4, 5].

To this end optical elastography techniques are particularly promising due to their non-invasive label free nature [6]. Brillouin light scattering (BLS) spectroscopy is one such approach that, owing in part to the realization of fast and sensitive BLS imaging spectrometers over the last decade [7], has been receiving renewed interest for

biomedical applications [8–18]. One challenge for exploring its usefulness in clinical settings is the required sample mounting on a microscope, which not only adds an extra level of complexity and required know-how by the user, but also may inadvertently affect the measured properties (due to the required excision and potentially modified chemical, physical and thermal conditions). To date the most notable translational progress of BLS has been for ophthalmological applications [19, 20]. However, the employed optical setups are specific for mapping the cornea in awake patients, and lack the versatility necessary for studying different tissue types [19, 20]. There has also been some progress towards realizing BLS endoscopes [21], however, these appear to still be in the early prototyping stages. This is due to the stringent design constraints for miniaturization, which are not only unnecessary but may also limit their versatility for rapidly assessing the properties of larger heterogeneous tissue (such as muscles and vasculature), where the average properties over extended areas and a high out-coupling efficiency to minimize tissue laser exposure, are desirable.

An important step towards exploring broader clinical applications would require a hand-held probe that can be operated by medical professionals and used directly in clinics for rapid *in situ* measurements of different tissue types. Here we introduce a robust and versatile fiber-coupled

* Corresponding author: kareem.elsayad@meduniwien.ac.at

hand-held BLS-spectroscopy probe with this in mind. We confirm its reliability by comparing standard confocal BLS microscopy measurements on the same excised soft tissues, and demonstrate that it can be used to reliably identify differences in the microscopic viscoelastic properties of different tissues as well as the same tissues at different sites. Our study here appears to present the first demonstration of such a device, as well as uncover previously unknown differences in the BLS viscoelasticity of various human tissue of direct biomedical interest under as close to homeostatic conditions as is possible without actually performing measurements on living persons.

## 1.1 BLS spectroscopy

Spontaneous BLS spectroscopy is a somewhat unique optical elastography approach, in that it measures the velocity of inherent GHz-frequency hypersonic waves (acoustic phonons) [22]. In its common microscopy implementation, it involves focusing a single frequency laser on a sample and measuring the resonant phonon scattering peaks. The frequency of these relative to the probing laser ($v_B$) is proportional to their velocity which can be used to calculate an elastic modulus [23]. In its most common implementation, BLS measures the complex *longitudinal* modulus $M = M' + iM''$. The elastic and dissipative components of the modulus ($M'$ and $M''$) can be extracted from the BLS-spectrum measured in the 180° back-scattering geometry, via [22]:

$$M' = \rho(v_B \lambda_0/2n)^2 \quad M'' = M' \cdot \Gamma_B/v_B. \quad (1)$$

Here $\rho$ and $n$ are the mass density and refractive index of the probed sample volume, $\lambda_0$ the free space wavelength of the probing laser, and $\Gamma_B$ the linewidth of the resonant BLS scattering peaks. This modulus is distinct from that obtained in most other elastography approaches, and it is worth taking a minute to revie1w this aspect, as it is relevant to the interpretation and potential applicability. $M$ is related to the shear modulus ($G$) and bulk modulus ($K$) via: $M = K + 4/3\ G$. $K$ represents a distinct mechanical property to $G$, that describes the compressibility of a material. Given liquids at physiological pressures are effectively incompressible ($K \approx 2.2$ GPa for water), $K$ in soft tissue will be very large, and the BLS measured modulus will be very sensitive to water content [24–26]. It will also be acutely sensitive to the nature of hydrostatic interactions between solid constituents and water [27, 28], which is a result of the fast (picosecond–nanosecond) mechanical relaxation processes that the probed GHz phonons are sensitive to. Variations in these due to *e.g.* cross-linking [7, 29] or cation screening [28, 30] will affect the dynamic hydrogen bond structure [31] and are reflected in the BLS measured modulus (as can be seen in the scaling of $M$ with respect to the solid-fraction and solute-properties [27, 28]).

Several studies have reported empirical correlations between the Atomic Force Microscopy (AFM)-measured tensile modulus, and the BLS-measured longitudinal modulus in different biological and biorelevant systems [32, 33]. While these likely indicate a common sensitivity to the properties and abundance of load bearing solid components, caution needs to be exercised when generalizing or extrapolating between the two. In light of the above, it is apparent that while the BLS measured $M$ might not always be relevant for describing the *macroscopic* mechanical properties of soft tissue, it is sensitive to the *microscopic* mechanical properties, which can have unique diagnostic value on account of their sensitivity to changes in hydration, chemical constituents and their interactions. It is, for example, well known that physiological function can be adversely affected by departures from homeostatic values of the water content and solute chemistry [34, 35], which can be indicative of different pathologies (*e.g.* cancer cells are understood to have a higher water content than their surrounding tissue [36]).

It is also apparent from the above that while in model systems, such as hydrogels or one/two-component mixtures, first-principle theoretical descriptions for changes in $M$ may be attempted [37], in complex biological soft tissue the dynamic interaction between the many constituents and microscopic structures make this challenging. As such from a medical applications perspective, a reverse engineering approach – where empirical associations with different pathologies, measured in a clinical setting, can ultimately prove most productive in expediting the path towards translation, *i.e.* by identifying diagnostically relevant factors that BLS is sensitive to.

The realization of an easy-to-use probe for *in situ* measurements would have distinct design requirements to those for imaging and endoscopy purposes. These include: (1) A single acquisition should measure an average over a suitably sized volume. This is necessary to avoid anomalies resulting from microscopic heterogeneities that "point" measurements are susceptible to. Homogeneously illuminating and detecting over a large probing volume has the undesirable effect of exposing the sample to high overall laser intensities. Alternatively, scanning a tightly focused point requires significant technical automation and compromises the technical complexity, robustness, cost and size. To this end the illumination and detection from a random or structured spatial pattern is desirable. (2) The probing laser intensity and acquisition time should be sufficiently low, so as to avoid perturbing the sample, and hence measurements by incurred photodamage and/or temperature changes. To this end a high coupling efficiency between the probe and spectrometer is desirable. In addition, features such as adequate suppression of elastic scattering and parallel or straight-forward sequential measurements on reference samples for spectral registration should also be addressed. (3) The measurement geometry should be such that the samples do not need to be excised and the user can obtain a measurement from one side, *e.g.* by simply pointing the probe at the region of interest. This, and to some extent also (2), negates the potential of using stimulated BLS which (at least in currently demonstrated implementations [38, 39]) requires measurement geometries not conducive to this. Finally, the potential to perform complimentary spectral analysis via *e.g.* Raman or (auto-) fluorescence measurements, is desirable, and the design should

thus also be suitable for (reasonably) broad-band excitation and detection.

## 2 Materials and methods

### 2.1 Tissue excision/prep

Human tissues were collected from the left upper limb of a male body donor, who, by free will had given written consent to donate his dead bodies to the Division of Anatomy of the Medical University of Vienna. His age at death was 77 years.

The muscles of the proximal forearm and the great subfascial arteries, veins and nerves were exposed using forceps and scalpel. Then 2 tissue samples (~$10 \times 5 \times 5$ mm$^3$) were harvested from muscles with longitudinal fiber arrangement (biceps brachii and pronator quadratus muscle), 2 from veins (brachial and medial cubital vein), 3 from muscular arteries (1 from brachial and 2 from radial artery), and 3 from the median nerve (1 from near its fork, 1 from distal to the pronator teres muscle, and 1 from distal to the carpal tunnel). The tissues were placed in phosphate buffered saline (PBS) until their further measurement by Brillouin scattering spectroscopy.

### 2.2 Hand-held probe

The housing of the hand-held probe was constructed from readily available opto-mechanical components available from commercial vendors (Thorlabs, Edmund Optics and Newport) together with custom printed 3D spacers. The entire probe measures approximately 150 mm $\times$ 200 mm, can be comfortably held in one hand and easily maneuvered to point at desired regions of interest. The basic optical principles are not too different from those of a conventional fiber-coupled Brillouin scattering confocal microscope [7], employing a polarizing beam splitter to couple in the probing laser (wavelength = 532 nm in our case) and a reference arm to measure a control sample for spectral registration. The latter can be instigated by a computer controlled mechanical shutter for on-the-fly spectral registration. While the quarter waveplates result in a circular polarized excitation at the sample, the scattering from longitudinal (polarization maintaining) modes will by far be dominant and this does not perturb the BLS signal compared to probing with a linear polarization and parallel analyzer in the back-scattering geometry employed. One key difference compared to a conventional confocal point detection scheme lies in the probing and acquisition optics, which is designed to acquire spectra from an extended region (2 mm) simultaneously (as opposed to a single point), and to maximize the light coupling efficiency out of the probe. In particular, the laser light is fed to the probe via a multimode fiber bundle (BF20HSMA02, Thorlabs) with stainless steel protective tubing. The output of the fiber-face is firstly roughly collimated and then passed through an anti-reflection coated polarizing beam splitter cube. While the output of the fibers is not entirely linearly polarized, the fraction coupled to the sample and to the

calibration arm can still be slightly adjusted using a half wave plate as shown in Figure 1A. The portion to the sample passes through a quarter waveplate, a relay lens system (30 mm focal length) L1 and L2, and imaged with a magnification of unity by an aspherical lens (L3) onto the sample with an effective NA of ~0.2. A custom mask/iris in the intermediate image plane (IP in Fig. 1A) can be used to modify the size of the probed area in the sample plane. Additionally, a mask in the infinity space (prior to relay lenses) may be used for Fourier filtering and modifying the "shape" of the probed points (not employed in the presented results). The back-scattered light from the sample, is coupled into an equivalent second multimode fiber bundle which runs to the BLS spectrometer. On the side of the BLS spectrometer the light was first passed through an iodine absorption cell coupled to the laser, and then demagnified by a relay system before being fed to the spectrometer. Spherical lenses (LA1116-A – LA1770-A and LA1540-A – LA1207-A, Thorlabs) with broad-band (350–700 nm) anti-reflection coatings were used in the probe. An adjustable custom-made metal spacer tube was mounted at the imaging tip of the probe, the length of which was set so that the sample position coincides with the probing/detection plane when the probe is brought in contact with the sample.

The Brillouin spectrometer employed was a cross-dispersion VIPA spectrometer (free spectral range 30 GHz at 532 nm) previously described [40], equipped with a heated iodine gas absorption cell for elastic scattering suppression [41] and a Lyot stop for removing parasitic high spatial-frequency components [42]. Excitation was via a 532 nm 750 mW single mode laser (Torus, Laser Quantum, Germany) with an optical isolator, electric shutter, and neutral density filter wheel, prior to being fiber coupled. The delivery to the probe was rather inefficient owing to the coupling efficiency to the fiber bundle, and subsequent polarization selection at the probe, however the out coupling was significantly higher than could be obtained with a single mode fiber setup. (Our most recent implementation employs a Dove prism on the detection arm of the probe–not used for obtaining the presented results–to perfectly align the probing and detection "points" with the fibers on the fiber bundle, and is able to improve the out-coupling efficiency by ~10–20%). The software-controlled laser current was tuned so that the probing laser frequency coincided with an absorption line of the heated gas cell. This was stabilized in quasi-real time, with the efficiency of elastic scattering suppression monitored by coupling out a small fraction of the scattered light in the spectrometer with a glass plate onto a single-pixel silicon photodetector. Acquisition was controlled via a Labview (National Instruments, USA) based program developed by THATec Innovations Inc. (Germany).

Data was analyzed using a custom Matlab (Mathworks, Germany) code which performed least squares fitting of two Lorentzian curves and spectral registration from reference sample data, as previously described [40]. We note that the BLS peaks are actually described by a Damped Harmonic Oscillator (DHO) [22], however the differences in the peak position as well as the line width (defined by
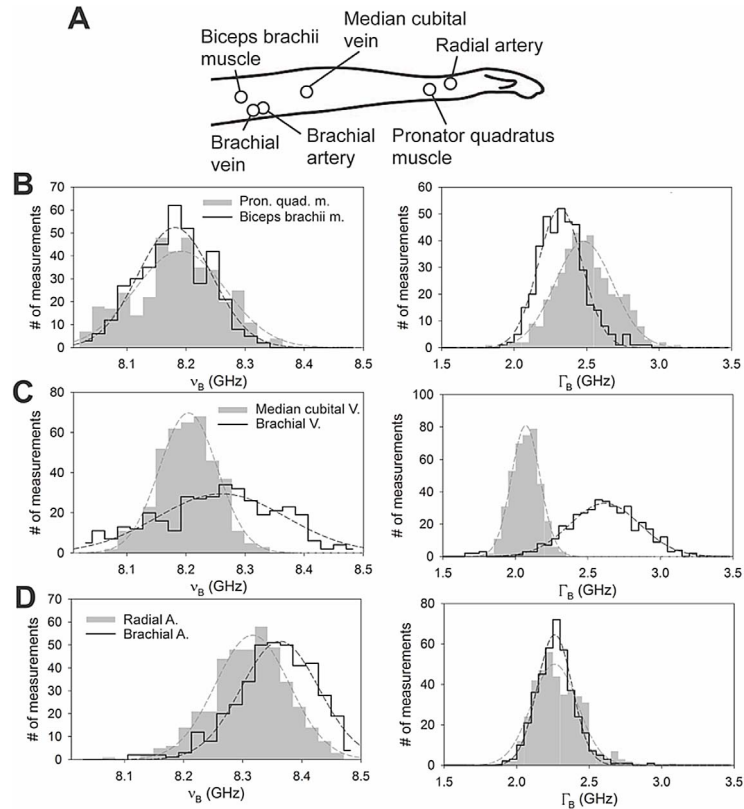
**Fig. 1.** (A) Sketch showing approximate location on arm of the excised tissues studied. (B–D) Distribution of BLS frequency shift ($v_B$) and linewidth ($\Gamma_B$) for the different tissue samples obtained from large-area confocal grid scans. Distributions are each fitted with a Gaussian distribution (dashed lines) and results are collated in Table 1.

the full width at half maximum) of fitting with a Lorentzian function versus a DHO were negligible and significantly smaller than other uncertainties. Prior to fitting, the sample spectra was deconvolved with a measurement of the attenuated elastic scattering peak obtained by holding the probe against a mirror, detuning the gas absorption cell resonance, attenuating the laser with a neutral density filter, and opening the intermediate image plane masks in the spectrometer. These measurements were only performed at the beginning of each measurement session. Owing to the symmetric response function, deconvolution did not make any noticeable difference to the peak position, and decreased the line width only by a small constant amount. As such, all conclusions from our studies would equally hold for non-deconvolved data. For calibration of the dispersion axis the simultaneously measured spectra of water (7.46 GHZ) and a previously characterized hard plastic (11.30 GHz) were placed in the cuvette on the sample arm in a manner that the detection–excitation area spanned both materials (see Fig. 1A). Calibration spectra were obtained prior to each sample measurement by opening and closing the shutters to the calibration and pointing the probe away from any sample (*e.g.* to the floor). A single programmed calibration measurement consisted of taking the average of five 500 ms measurements, lasted a couple of seconds, and could be instigated by a single click in the software.

Measurements on samples were performed by placing freshly excised tissue samples in a petri dish with Phosphate Buffered Saline (PBS) heated at 37 °C, and holding the probe directly against (in contact with) the sample. Acquisition was triggered by opening the shutter in front of the laser for the extent of the camera acquisition time. As such the sample would never be illuminated longer than the acquisition time. The entire acquisition process could be instigated by the single click of a shutter button connected to the computer that can also be held by the user. The laser power used for measurements on tissue were 10–25 mW (at the sample) and acquisition times were 100–750 ms (adjusted to obtain spectra with adequate signal to noise). We note that this variability in the acquisition times and laser power does not affect the result in regard to inducing any tissue damage/change (we are only performing a single measurement, and comparable laser exposure for orders of magnitude longer times is routinely used in spontaneous BLS confocal microscopy of live tissue with no adverse side effects [32]). The dispersion of the VIPA spectrometer in all our measurements was tuned such that the BLS peaks populated ~10 pixels on the EM-CCD camera (with the EM gain set at a maximum value of 1200). This number can easily be reduced or increased to an optimal value depending on the desired accuracy with which one wishes to extract the BLS-peak/linewidth, the photon statistic/acquisition times, and any other constraints, and may in

general want to be optimized on an application/sample specific basis before clinical translation. Each single measurement by design effectively gathers the average spectrum from 7 points simultaneously spread over ~2 mm of the sample (as shown in Fig. 1A inset). This serves to effectively mitigate the contribution from local artifacts that may arise in single-point measurements and gives an average spectra for the probed area (see above and below). Consecutive measurements on the same sample were performed by lifting the probe and placing it into contact with a spatially displaced region of the sample chosen at random. All measurements were performed at least 1 mm away from the edge of the excised sample and within minutes of each other on a given sample.

## 2.3 Scanning confocal Brillouin microscopy

Measurements were performed using the same double-VIPA spectrometer as for the hand-held probe, but this time coupled (using a single-mode fiber) to an inverted microscope (iX-73, Olympus, Japan) equipped with a sample scanning motor stage (ASI, USA) and 3-axis piezo stage (Physik Instrumente, Germany) described previously [40]. The same freshly excised samples were placed in high-precision glass-bottom dishes (Matek, Slovak Republic), immersed in PBS and kept at 37 °C with a microscope-top heater (Ibidi, Germany) throughout the experiments. A 1.2 NA 60× immersion objective (Olympus, Japan) was used, however an iris in the infinity space behind the objective cropped the probing/detection beam to yield a calculated numerical aperture of 0.2–0.3 (comparable to the numerical aperture of the hand-held probe). Prior to coupling the detected light into the fiber leading to the spectrometer, it was expanded using a relay lens system to assure that the effective fiber-pinhole was 1–2 Airy units. Spatial scans consisted of coarsely scanning a square grid of 2 mm with the motor stage translating the sample. Spectral fitting was all performed using Matlab (Mathworks, Germany) as described in [40]. The distribution of Brillouin frequency shifts and linewidths of the voxels were then collated and binned using a custom Matlab script. Statistical analysis and comparisons were performed using Sigmaplot (Systat Software Inc., Germany).

## 3 Results

BLS confocal scanning microscopy measurements of freshly excised tissue, in PBS and heated to 37 °C were performed as described in Section 2. Figure 1A shows the approximate position on the arm of the excised tissue. The distribution of the measured BLS frequency shift for the different studied tissue are shown in Figures 1B–1D. The complex longitudinal modulus is calculated using equation (1), with values from the literature for the refractive index and density of (1.42 and 1.05 g/cm$^3$ for the muscles, and 1.43 and 1.06 g/cm$^3$ for the veins and arteries) [43–45], and presented in table 1. The studied arteries are seen to have a higher BLS frequency shift ($\nu_B$) and longitudinal storage modulus ($M'$) than the veins, which in turn have a higher

**Table 1.** Mean BLS frequency shift ($\nu_B$), linewidth ($\Gamma_B$) and longitudinal modulus ($M'$, $M''$) for confocal BLS microscopy scans of excised human tissue, extracted from Gaussian fits of the distributions shown in Figure 1. $\sigma$ are the respective standard deviations (spread), and s.e. the standard errors for the fits. The last two columns show the mean values of $\nu_B$ and $M'$ obtained for measurements using the hand-held probe (Fig. 2) together with their respective standard deviation $\sigma$.

| | $\nu_B$ (s.e.) GHz | $\sigma_{\nu_B}$ (s.e.) GHz | $M'$ ($\sigma_{M'}$) GPa | $\Gamma_B$ (s.e.) GHz | $\sigma_{\Gamma_B}$ (s.e.) GHz | $M''$ ($\sigma_{M''}$) GPa | probe $\nu_B/\sigma_{\nu_B}$ GHz | probe $M'/\sigma_{M'}$ GPa |
|---|---|---|---|---|---|---|---|---|
| Pronator quadratus muscle (PQM) | 8.190 (0.003) | 0.076 (0.003) | 2.471 (0.046) | 2.480 (0.004) | 0.200 (0.004) | 0.748 (0.067) | 8.213/0.008 | 2.485/0.004 |
| Biceps brachii muscle (BBM) | 8.181 (0.002) | 0.063 (0.002) | 2.466 (0.038) | 2.318 (0.003) | 0.152 (0.003) | 0.644 (0.047) | 8.189/0.019 | 2.471/0.012 |
| Median cubital vein (MCV) | 8.204 (0.001) | 0.049 (0.001) | 2.469 (0.029) | 2.071 (0.001) | 0.099 (0.001) | 0.623 (0.034) | 8.220/0.008 | 2.478/0.005 |
| Brachial vein (BV) | 8.260 (0.004) | 0.109 (0.004) | 2.502 (0.066) | 2.617 (0.005) | 0.241 (0.005) | 0.793 (0.085) | 8.264/0.016 | 2.505/0.010 |
| Radial artery (RA) | 8.317 (0.001) | 0.063 (0.001) | 2.537 (0.038) | 2.261 (0.005) | 0.159 (0.005) | 0.796 (0.062) | 8.308/0.012 | 2.532/0.007 |
| Brachial artery (BA) | 8.363 (0.001) | 0.066 (0.001) | 2.565 (0.040) | 2.262 (0.002) | 0.120 (0.002) | 0.804 (0.049) | 8.371 (0.016) | 2.570 (0.010) |
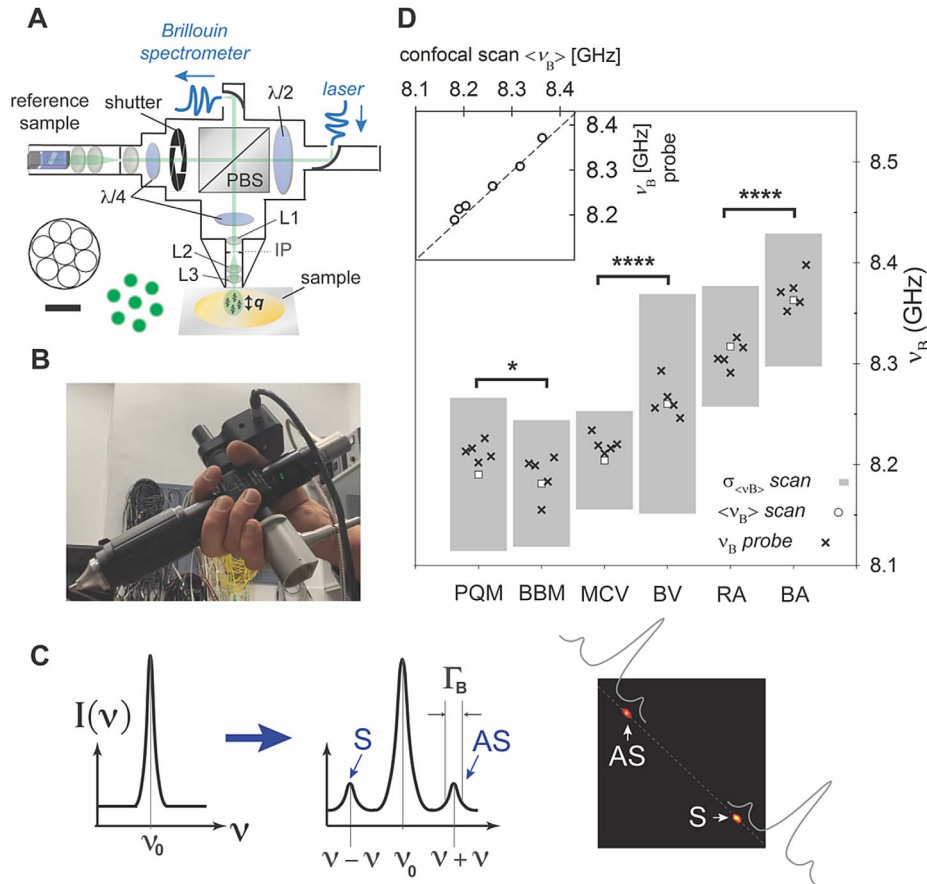
**Fig. 2.** (A) Schematic of the hand-held BLS probe (PBS = Polarizing Beam Splitter; $\lambda/4$ = quarter waveplate; $\lambda/2$ = half waveplate; IP = intermediate image plane; L1 & L2 relay lenses; L3 focusing lens; $q$ = predominant phonon-scattering wavevector probed in the sample). Inset shows a sketch of the multimode fiber bundle cross section used for coupling light into and out of the probe, and the excitation pattern projected onto sample (green dots). Scale bar = 1 mm. (B) Photograph of hand-held probe. (C) Example of BLS-spectra showing Stokes (S) and Anti-Stokes (AS) BLS scattering peaks shifted by frequencies $\pm v_B$ relative to the probing laser frequency $v_0$. Also shown is an example of a raw spectral projection measured with the BLS imaging spectrometer using the hand-held probe (dashed line = dispersion axis). (D) BLS measurements on the same samples as in Figure 1 using the hand-held probe (**x**). Also shown are mean values ($\square$) and the standard deviation of the mean (grey bars) of the confocal scan measurements (*viz.* Fig. 1 and Table 1). Inset: Mean $v_B$ obtained from confocal scan measurements versus that obtained using the hand-held probe (later is average of 5 measurements). Statistical differences are for $v_B$ of the different tissues measured using the hand-held probe, and were performed using unpaired $t$-test's with Welch's correction (*$p < 0.05$, ****$p < 0.0001$). Sample acronyms are as defined in Table 1.

value than the skeletal muscles studied (Figs. 1B–1D). We also observe a notable difference between the specific types of arteries and veins, with the *Brachial artery* and *Brachial vein* both having a notably higher $v_B$ and $M'$ (Figs. 1C and 1D respectively). In Figures 1B–1D we also show the corresponding linewidth distributions of each of the excised tissue which are related to the loss modulus (Eq. (1)) and longitudinal viscous properties (see below).

In order to check the reliability of the hand-held probe we performed measurements on each of the same samples under the same conditions using the hand-held probe. A schematic and photograph of the hand-held probe is shown in Figures 2A and 2B, and described in detail in Section 2. An example of a characteristic raw spectral projection measured using the employed imaging spectrometer with the hand-held probe is shown in Figure 2C. The results of the BLS frequency shift were in each case compared to what

was obtained from the confocal scans (*viz.* Figs. 1B–1D) and are presented in Figure 2D. All measurements with the hand-held probe fall close to the mean value of the normally distributed values collated from the confocal scans of each sample, with the standard deviation over repeated measurements (column 9, Table 1) significantly smaller than that extracted from histograms of confocal scans (Fig. 1; column 4, Table 1). This confirms that the hand-held probe is effective in obtaining spatially averaged values and not significantly skewed by outliers resulting from local spatial heterogeneities. That the hand-held probe can from just a few measurements (5 in our case) obtain the same average values as a fine confocal scan (many hundreds of pixels) is evident by directly comparing the mean values obtained using the two detection approaches, shown in the inset of Figure 2D. Statistical analysis of the measurements performed using the hand-held probe (Fig. 2D)
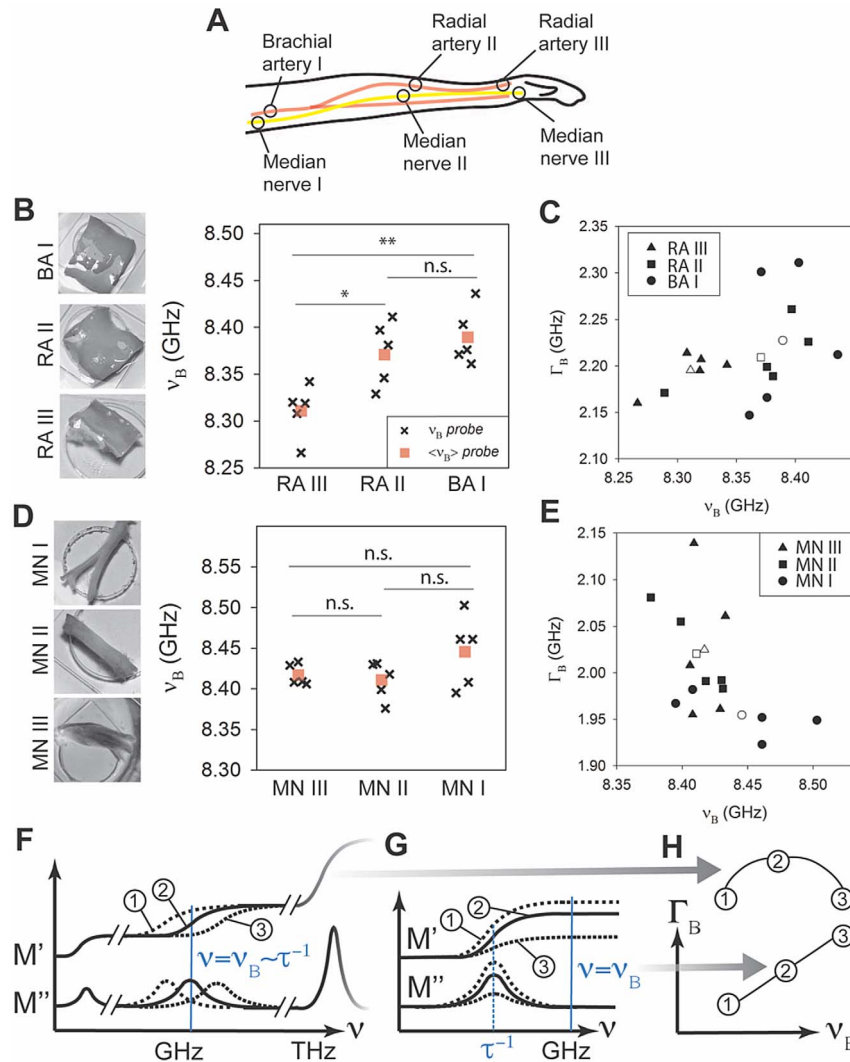
**Fig. 3.** (A) Sketch showing approximate locations along the arm of the excised tissues studied. (B and D) Collated results of independent measurements of $v_B$ (**x**) using the hand-held probe at different positions of the *Brachial/Radial artery* (BA/RA) and *Median nerve* (MN) as indicated in "A" (■ = mean of 5 measurements). (C and E) Corresponding plots of $\Gamma_B$ versus $v_B$. (Solid symbols = individual measurements; open symbols = mean; dashed line = trend line of mean). In (C) the Pearson correlation coefficient for the individual measurements is 0.46, whereas for (E) it is $-0.53$. (F and G) Expected frequency dispersion of the complex modulus $M = M' + iM''$ when probing (F) a heterogeneous sample with different relaxation times ($\tau$) in the vicinity of $\tau \sim v_B^{-1}$, and (G) the effect of different strengths of a relaxation process with $\tau > v_B^{-1}$ as may occur for different solid fractions. (H) Sketch of the expected scaling of $\Gamma_B$ with respect to $v_B$ for the two scenarios. Statistics performed using unpaired *t*-test with Welch's correction (*$p < 0.05$, **$p < 0.01$).

confirm that these can serve to reliably distinguish the different tissue types.

The hand-held probe can also be used to identify changes in properties of the same tissue-type at different locations. This is shown in Figures 3A–3E where we measure the BLS frequency shift and linewidth of the *Brachial/Radial artery* (BA/RA) and *Median nerve* (MN) at different positions along the arm (indicated on the sketch in Fig. 3A). As can be seen in Figures 3B and 3D, the BLS frequency shift $v_B$ for the artery appears to slightly increase moving up the arm (towards the torso), while that of the nerve does not show a significant difference. The change in the linewidths $\Gamma_B$ with respect to the

frequency shifts $v_B$ are shown in Figures 3C and 3E. These plots (which reveal how the *viscous* longitudinal properties scale with respect to the *elastic* longitudinal properties), appear to follow distinct trends in the two tissues (Pearson correlation coefficient 0.46 vs. $-0.53$), which may be indicative of different underlying mechanical relaxation time spectra, as discussed below.

The shape of the Point Spread Function (PSF) is an important factor in that it will determine the structural features one is sensitive to and define the scattering wavevectors probed. This can (as described above) be tuned in our hand held probe. In our implementation the excitation PSF will essentially resemble the output from the fibers, and

consist of 7 separated points, and one is thus probing an area over hundreds of microns. The shape of the true effective PSF (excitation × detection) is less trivial, and will depend on the (angular) alignment of the excitation–detection fiber bundles (which is optimized manually as best possible to achieve a maximum through put/coupling). In practice for heterogeneous and anisotropic tissue this is additionally complicated on several levels, starting with the fact that the BLS scattering cross section will be dependent on such structure, and ending in that the coupling efficiency into the fibers will depend on the wavefronts which will also be perturbed. In between one has the effects of multiple scattering in the sample, and as such measurements thereof, which are important for understanding what is really probed, should be undertaken on an application specific basis.

## 4 Discussion

Of the measured samples, we find artery walls have a higher storage modulus $M'$, than those of veins, which in turn have a higher modulus than skeletal muscle tissue. Except for the *Median cubital vein* (MCV), the loss modulus $M''$ show the opposite trend. It is well known that veins are significantly more compliant than arteries [46], namely that under a given pressure they will deform more, and the observed reduction in $M'$ may be a manifestation of this. It is also worth noting that quasi-static tensile and shear measurements have also reported an increased modulus of arteries compared to veins, which is in turn larger than that of skeletal muscles [47, 48]. Our results suggest that $v_B$ for nerves (Figs. 3D and 3E) is notably larger than that of skeletal muscles, veins and arteries (which translates also to a higher $M'$ taking the refractive index and mass density of nerves [49] as 1.40 and 1.075 g/cm$^3$) – a trend that is also observed for the lower frequency shear and tensile moduli [50]. As such, for all the probed tissue types, $M'$ follows a similar trend to the quasi-static tensile storage modulus. This qualitative similarity needs to however be interpreted cautiously, due to the many differences (boundary conditions, frequency regime – see above) associated with BLS measurements. It can however be argued that the load bearing components in solid-like tissue will have characteristic mechanical relaxation times much slower than the GHz probed frequencies [23], and as such changes in the solid-structure or abundance of solid constituents would manifest themselves in both the BLS measured modulus and the quasi-static tensile modulus. The relative change would however be expected to be significantly smaller in the BLS modulus, given the sizable liquid bulk contribution (as is indeed observed).

The feasibility of the hand-held probe to measure an averaged spectra over an extended area is evident from Figure 2D, with all the measurements falling close to the mean obtained in conventional confocal scan measurements (Fig. 2D inset). These measurements are seen to also be able to reliably differentiate the different tissues (Fig. 2D), which would not be possible from single point measurements. This is particularly important for measuring heterogeneous soft tissue, where the BLS spectra may vary spatially, yet have an average that differs only slightly from sample to sample. It is worth mentioning that heterogeneities in the mechanical properties of the probed tissues are not exclusive to BLS, and also evident in *e.g.* AFM measurements [51]. While the distributions in Figure 1 are all reasonably well described by a normal distribution (suggesting a sufficiently large number of data points were probed to account for tissue heterogeneity), for the case of the *Pronator quadratus muscle*, as well as possibly the *Brachial artery*, there are hints of a potential bimodal distribution. These are not evident in measurements from the hand-held probe, which yield a value close to the single-distribution mean (Fig. 2D), suggesting that the probe measurements are effective in averaging out such spatial heterogeneities.

Our results using the hand-held probe also show that it is possible to observe changes in the BLS modulus within the same tissue at different locations. For the *Brachial/ Radial artery* we find an increased BLS frequency shift $v_B$ further up the arm (Fig. 3B), which may be tied to the higher pressures that larger arteries are subject to. In the *Median nerve* no such trend is apparent (Fig. 3D). The scaling of the longitudinal elastic to viscous properties (as can be seen by plotting $v_B$ against $\Gamma_B$) reveal a significant difference between the *Brachial/Radial artery* and the *Median nerve* (Figs. 3C and 3E). It is not possible to deduce the origins of this in regard to differences in the mechanical relaxation spectrum [23, 30, 31], without systematically perturbing the sample [27] (via changing *e.g.* the temperature, hydration, etc.) or performing correlative measurements at different frequencies, which both lie beyond the scope of this proof-of-principle study. We note however that a decrease in the BLS linewidth with respect to the BLS frequency shift (as is seen for the *Median nerve*, Fig. 3E) may be the result of the BLS probed frequency being just above a pronounced relaxation process $v_B > \tau^{-1}$ (where $\tau$ is the characteristic relaxation time). This would result in a frequency dispersion of the complex modulus $M$ shown in Figure 3F, and $M''$ decreasing with increasing $M'$ [11, 23] ("2"–"3" in Fig. 3H). On the other hand, an increase in the BLS linewidth with respect to the BLS frequency shift (as is seen for the *Brachial/Radial artery*, Fig. 3C), could be the result of either being just below such a relaxation process [11] $v_B < \tau^{-1}$ (Fig. 3F and "1"–"2" in Fig. 3H) or alternatively due to a relative increase in a solid constituent with a slower characteristic relaxation time (which would be the case also for different levels of hydration [24–26]). Figures 3G and 3H show how the latter would affect the frequency dispersion of $M$ and the resultant scaling of $M''$ relative to $M'$.

To date numerous studies have suggested the BLS modulus may have medical diagnostic value [9, 11–18]. In regard to the tissues studied here, BLS confocal microscopy studies assessing plaque stiffness in carotid arterial histological sections have shown that BLS is sensitive to "stiffening" in mouse models [12], while studies on muscle fibrils have revealed a correlation to loss of function observed in certain mutations [13]. A very nice comprehensive study on diverse tissues has also shown clearly distinguishable differences between tissue types [52], which is encouraging in terms

of its applicability for diagnosing pathological anomalies in a broader context. One can speculate that since collagen and elastin exhibit distinct BLS moduli [24], BLS may provide a measure of age related arterial "stiffening" (which is associated with an increased collagen to elastin ratio [3]). Given the similar trends observed by the BLS measured $M'$ and the quasi-static tensile modulus, it would thus be interesting to see if BLS is also sensitive to the progression of diseases such as atherosclerosis *in situ*, which is associated with changes in the collagen network (packing) morphology, that has been detected with AFM [53]. In such cases, BLS performed using the presented probe could provide a clear practical advantage, as it can potentially be used directly in the clinic without the need for excision. An important aspect of our studies here was that the tissue was both freshly excised, in isotonic media, and at 37 °C, thus as closely mimicking its natural state as was possible. To this end variation due to hydration (which BLS is acutely sensitive to) would only differ in so much as they differ in the native living tissue, and our results presented here reflect what can reasonably be expected to be obtained from *in situ* studies.

We have for the most part focused largely on the frequency shift $v_B$ (and corresponding $M'$) as opposed to the linewidth $\Gamma_B$ (and loss modulus $M''$), which will be addressed more thoroughly in a future communication. We note here though, that while more challenging to extract correctly with imaging spectrometers [8], the potential usefulness of $M''$ is becoming increasingly apparent, with relative changes (as a result of incurred structural changes) often more pronounced than those of the storage modulus $M'$ in soft matter [27, 54]. This is also apparent in Figures 1B–1D and Figures 3C and 3E, and understandable considering the dispersion of $M''$ in Figures 3F and 3G. To appreciate why this might be the case, we note that the loss properties are related to the longitudinal viscosity $\eta_L$ via: $M'' \approx 2\pi v_B \eta_L$. $\eta_L$ is distinct from the shear viscosity $\eta_S$ in that $\eta_L = \eta_B + (4/3)\eta_S$, where $\eta_B$ is the *bulk* or *second* viscosity [55]. $\eta_B$ is understood to be a material independent property [55] that like the bulk modulus $K$ will in practice mainly be significant only for describing deformations under high pressures/impulses or longitudinal wave propagation [55] and to our knowledge, at least not directly, significant for physiological deformations in soft matter. Since the contribution from $\eta_B$ will typically be of the same order of magnitude as the shear component [56], relative variations in $\eta_L$ will reflect changes of $\eta_S$ in soft matter. While at quasi-static frequencies the elastic properties will be largely defined by the load bearing components, the viscous properties will be governed by *liquid* component (*e.g.*, interstitial fluid). As such, though still at a much higher frequency, $\eta_L$ may serve as a proxy for describing changes in the viscous properties at physiological conditions. Accurate extraction of $\Gamma_B$ (and hence $M''$), generally requires, in addition to spectral deconvolution, detailed consideration of the range of scattering wavevectors probed [57] and the effects from multiple-scattering [58]. For our current studies the former would not cause a significant change in $v_B$ due to the relatively small numerical aperture and backscattering geometry, while the latter can also be assumed negligible

as we are measuring near the sample surface, and these have thus both not been accounted for.

A potential issue of the current design of the hand-held probe (which is also relevant for BLS spectroscopy/ microscopy and indeed most mechanical testing techniques) is that the mechanical properties are measured in a given direction. As such, in tissue with anisotropic mechanical properties, measurements will be sensitive to the direction from which the tissue is probed. While typically associated with "hard" tissue, mechanical anisotropy is also significant in soft tissue such as muscles [24, 26] and can be expected from any tissue with an underlying anisotropic load bearing structure. Given that our results are obtained using a relatively low NA and that in BLS measures the modulus in the direction of the scattering wavevector $\boldsymbol{q}$, our measurements can be considered to probe the mechanical properties in the direction that the probe is pointed. To overcome this directional bias, one can consider a design that measures an average over different $\boldsymbol{q}$ with high-NA collection and/or detection optics. However, in doing so one compromises the ability to reliably extract the BLS linewidth [57] (and hence the viscous component of the modulus). As such, a choice needs to be made whether to focus on angular-averaged properties, the linewidth (longitudinal viscosity), or a more elaborate design that consecutively/serially measures spectra for different $\boldsymbol{q}$ (but likely compromises the fast measurement capabilities). It is worth noting that the refractive index may in of itself also be anisotropic, with the refractive index appearing in equation (1) being that in the direction of the scattering wavevector.

The refractive index and density may in of themselves also be significantly perturbed in different pathologies [43], thereby affecting the calculated $M$ (Eq. (1)). While using literature values may to a first approximation offer a material-type specific correction that gets one closer to the microscopic mechanical properties, it may for prognostic and diagnostic purposes prove to be desirable to work with the frequency shift and linewidth (or normalizations thereof [8, 59]) when these parameters are not available (as is currently done in ophthalmological translational applications [20]). On the one hand complimentary measurements to extract these may be employed [60], however how these would translate to applications using a hand-held probe is unclear. To this end the mechanical loss tangent, defined as $\tan \delta = \Gamma_B / v_B = M'' / M'$, can also serve as a convenient means of excluding the explicit dependence on refractive index and mass density, and has been suggested can provide a measure of the "fluidity" in BLS imaging applications [61]. The potential usefulness of this parameter is the subject of current investigations and will be reported for tissue-specific studies in subsequent communications.

The sensitivity of the probe is dependent ultimately on the fiber coupling efficiency. We routinely can achieve >50%, however, this is dependent on the wavefront deformation due to the sample, and as such this will be tissue and region specific. This affects the accuracy with which the BLS peak position and line width can be determined, since this is primarily a localization problem, not unlike that in super-resolution localization microscopy, with comparable scaling with respect to photon statistics. To this end

the use of multimode fibers certainly helps, however we note that some light is additionally lost on the spectrometer side due to mode cleanup prior to entering the VIPA's (see above). The photon statistics will also depend on the Brillouin scattering cross section, namely intrinsic material properties, and will be affected also by the transparency of the tissue (which would affect the size of the effective point spread function). As such the issue of sensitivity and accuracy needs to be approached in a sample/application specific manner, considering also the maximum laser power that the specific tissue can be exposed to before causing irreversible damage or affecting its properties. In VIPA spectrometers one can adjust the number of pixels over which the peak is spread on the EM CCD camera (and thereby the number of photons per pixel) by changing the VIPA tilt, and this may also be optimized in an application specific manner to allow for the maximum signal with the minimum required accuracy. In our case the uncertainty in the parameters was significantly smaller than the statistical sample-to-sample variability and could thus be neglected. We note that ultimately the resolution of the spectrometer will also come into play (despite spectral deconvolution), however this is generally much smaller than that from the statistical uncertainty of different samples and can thus also be safely ignored.

Finally, it needs to be emphasized that while our results are based on multiple measurements on different regions of tissue, they are from a single person. While this is an essential first step in developing and optimizing suitable probes, to draw general conclusions would require measurements from many people.

# 5 Summary and outlook

In summary, we have introduced and demonstrated the feasibility of a robust hand-held BLS probe for studying various freshly excised human tissue, that can readily also be applied for anatomical studies as well as potentially in clinics. A key feature of the probe is that it acquires the average spectra over an extended spatial area, in a single ($<1$ s) measurement. It does so by simultaneously illuminating a pattern of spots in the sample, and yields a value of $v_B$ in good agreement with the mean value from more-timely confocal microscopy scans of the same samples. We show this allows one to distinguish different tissue types with a single shot measurement and minimal laser exposure (which would not be possible from a point measurement given the heterogeneous properties of many tissues). While the probing area in our implementation is approximately 2 mm in diameter, this can readily be modified by changing the focal length of the relay lenses in the probe. For certain application this instantaneous averaging feature may not be desirable, in which case more elaborate scanning probes need to be realized. Though the aim of this study was a proof-of-principle demonstration of the hand-held probe, we in doing so also obtain insight into the properties of different tissues, that may form the basis of future investigations. For example, our results for vasculature suggest the storage modulus $M'$ increases further up the arm (towards

the torso). We also observe that the measured BLS moduli of skeletal muscles, veins, arteries and nerves appear to follow a similar trend to what is observed in quasi-static tensile measurements (*i.e.,* are largest for nerves and smallest for skeletal muscles). Despite the clear difference in the moduli probed, this is promising in so far that it may mean that variations of the BLS measured moduli could also be sensitive to pathological abnormalities associated with changes in the quasi-static tensile mechanical properties. To what extent BLS can prove useful for classifying the health of tissue and assessing pathologies in clinical settings however remains to be seen, and the introduced hand-held probe offers a tool suitable for further investigating this *in situ.*

# Conflict of interest

The authors declare no conflict of interest.

# References

1 Ayad N.M.E., Kaushik S., Weaver V.M. (2019) Tissue mechanics, an important regulator of development and disease, *Philos. Trans. Roy. Soc. B: Biol. Sci.* **374**, 20180215. https://doi.org/10.1098/rstb.2018.0215.

2 Mukund K., Subramaniam S. (2020) Skeletal muscle: A review of molecular structure and function, in health and disease, *WIREs Syst. Biol. Med.* **12**, e1462. https://doi.org/10.1002/wsbm.1462.

3 Shirwany N.A., Zou M.-H. (2010) Arterial stiffness: A brief review, *Acta Pharmacol. Sin.* **31**, 1267–1276. https://doi.org/10.1038/aps.2010.123.

4 Spronck B., Humphrey J.D. (2019) Arterial stiffness: Different metrics, different meanings, *J. Biomech. Eng.* **141**, 0910041–09100412. https://doi.org/10.1115/1.4043486.

5 Bilston L.E., Tan K. (2015) Measurement of passive skeletal muscle mechanical properties in vivo: Recent progress, clinical applications, and remaining challenges, *Ann. Biomed. Eng.* **43**, 261–273. https://doi.org/10.1007/s10439-014-1186-2.

6 Kennedy B.F., Wijesinghe P., Sampson D.D. (2017) The emergence of optical elastography in biomedicine, *Nat. Photon.* **11**, 215–221. https://doi.org/10.1038/nphoton.2017.6.

7 Scarcelli G., Yun S.H. (2007) Confocal Brillouin microscopy for three-dimensional mechanical imaging, *Nat. Photon.* **2**, 39–43. https://doi.org/10.1038/nphoton.2007.250.

8 Antonacci G., Beck T., Bilenca A., Czarske J., Elsayad K., Guck J., Kim K., Krug B., Palombo F., Prevedel R., Scarcelli G. (2020) Recent progress and current opinions in Brillouin microscopy for life science applications, *Biophys. Rev.* **12**, 615–624. https://doi.org/10.1007/s12551-020-00701-9.

9 Poon C., Chou J., Cortie M., Kabakova I. (2021) Brillouin imaging for studies of micromechanics in biology and biomedicine: from current state-of-the-art to future clinical translation, *J. Phys.: Photon.* **3**, 012002. https://doi.org/10.1088/2515-7647/abbf8c.

10 Elsayad K., Polakova S., Gregan J. (2019) Probing mechanical properties in biology using Brillouin microscopy, *Trends Cell Biol.* **29**, 608–611. https://doi.org/10.1016/j.tcb.2019.04.002.

11 Mattana S., Caponi S., Tamagnini F., Fioretto D., Palombo F. (2017) Viscoelasticity of amyloid plaques in transgenic mouse brain studied by Brillouin microspectroscopy and correlative Raman analysis, *J. Innov. Opt. Health Sci.* **10**, 1742001. https://doi.org/10.1142/S1793545817420019.

12 Antonacci G., Pedrigi R.M., Kondiboyina A., Mehta V.V., De Silva R., Paterson C., Krams R., Török P. (2015) Quantification of plaque stiffness by Brillouin microscopy in experimental thin cap fibroatheroma, *J. R. Soc. Interf.* **12**, 20150843. https://doi.org/10.1098/rsif.2015.0843.

13 Cikes D., Elsayad K., Sezgin E., Koitai E., Ferenc T., Orthofer M., Yarwood R., Heinz L.X., Sedlyarov V., Miranda N.D., Taylor A., Grapentine S., al-Murshedi F., Abott A., Weidinger A., Kutchukian C., Sanchez C., Cronin S.J.F., Novatchkova M., Kavirayani A., Schuetz T., Haubner B., Haas L., Hagelkruys A., Jackowski S., Kozlov A., Jacquemond V., Knauf C., Superti-Furga G., Rullman E., Gustafsson T., McDermot J., Lowe M., Radak Z., Chamberlain J.S., Bakovic M., Banka S., Penninger J.M. (2022) Critical role of PCYT2 in muscle health and aging, *bioRxiv*, 2022.2003.2002.482658. https://doi.org/10.1038/s42255-023-00766-2.

14 Conrad C., Gray K.M., Stroka K.M., Rizvi I., Scarcelli G. (2019) Mechanical characterization of 3D ovarian cancer nodules using Brillouin confocal microscopy, *Cell Mol. Bioeng.* **12**, 215–226. https://doi.org/10.1007/s12195-019-00570-7.

15 Rix J., Uckermann O., Kirsche K., Schackert G., Koch E., Kirsch M., Galli R. (2022) Correlation of biomechanics and cancer cell phenotype by combined Brillouin and Raman spectroscopy of U87-MG glioblastoma cells, *J. Roy. Soc. Interf.* **19**, 20220209. https://doi.org/10.1098/rsif.2022.0209.

16 Zhang J., Raghunathan R., Rippy J., Wu C., Finnell R.H., Larin K.V., Scarcelli G. (2019) Tissue biomechanics during cranial neural tube closure measured by Brillouin microscopy and optical coherence tomography, *Birth Defects Res.* **111**, 991–998. https://doi.org/10.1002/bdr2.1389.

17 Riobó R.J.J., Gontán N., Sanderson D., Desco M., Gómez-Gaviro M.V. (2021) Brillouin spectroscopy: From biomedical research to new generation pathology diagnosis, *Int. J. Mol. Sci.* **22**, 8055.

18 Troyanova-Wood M., Meng Z., Yakovlev V.V. (2019) Differentiating melanoma and healthy tissues based on elasticity-specific Brillouin microspectroscopy, *Biomed. Opt. Express* **10**, 1774–1781. https://doi.org/10.1364/BOE.10.001774.

19 Besner S., Scarcelli G., Pineda R., Yun S.H. (2016) In vivo Brillouin analysis of the aging crystalline lens, *Invest. Ophthalmol. Vis. Sci.* **57**, 5093–5100. https://doi.org/10.1167/iovs.16-20143.

20 Scarcelli G., Yun S.H. (2012) In vivo Brillouin optical microscopy of the human eye, *Opt. Express* **20**, 9197–9202. https://doi.org/10.1364/OE.20.009197.

21 Kabakova I., Xiang Y., Paterson C., Török P. (2017) Fiber-integrated Brillouin microspectroscopy: Towards Brillouin endoscopy, *J. Innov. Opt. Health Sci.* **10**, 1742002. https://doi.org/10.1142/S1793545817420020.

22 Berne B.J., Pecora R. (2000) *Dynamic light scattering: With applications to chemistry, biology, and physics*, Dover Publications, New York, USA.

23 Palombo F., Fioretto D. (2019) Brillouin light scattering: Applications in biomedical sciences, *Chem. Rev.* **119**, 7833–7847. https://doi.org/10.1021/acs.chemrev.9b00019.

24 Palombo F., Winlove C.P., Edginton R.S., Green E., Stone N., Caponi S., Madami M., Fioretto D. (2014) Biomechanics of fibrous proteins of the extracellular matrix studied by Brillouin scattering, *J. R. Soc. Interf.* **11**, 20140739. https://doi.org/10.1098/rsif.2014.0739.

25 Wu P.J., Kabakova I.V., Ruberti J.W., Sherwood J.M., Dunlop I.E., Paterson C., Török P., Overby D.R. (2018) Water content, not stiffness, dominates Brillouin spectroscopy measurements in hydrated materials, *Nat. Methods* **15**, 561–562. https://doi.org/10.1038/s41592-018-0076-1.

26 Andriotis O.G., Elsayad K., Smart D.E., Nalbach M., Davies D.E., Thurner P.J. (2019) Hydration and nanomechanical changes in collagen fibrils bearing advanced glycation endproducts, *Biomed. Opt. Express* **10**, 1841–1855. https://doi.org/10.1364/BOE.10.001841.

27 Bailey M., Alunni-Cardinali M., Correa N., Caponi S., Holsgrove T., Barr H., Stone N., Winlove C.P., Fioretto D., Palombo F. (2020) Viscoelastic properties of biopolymer hydrogels determined by Brillouin spectroscopy: A probe of tissue micromechanics. *Science*, *Advances* **6**, eabc1937. https://doi.org/10.1126/sciadv.abc1937.

28 Adichtchev S.V., Karpegina Y.A., Okotrub K.A., Surovtseva M.A., Zykova V.A., Surovtsev N.V. (2019) Brillouin spectroscopy of biorelevant fluids in relation to viscosity and solute concentration, *Phys. Rev. E* **99**, 062410. https://doi.org/10.1103/PhysRevE.99.062410.

29 Scarcelli G., Kling S., Quijano E., Pineda R., Marcos S., Yun S.H. (2013) Brillouin microscopy of collagen crosslinking: noncontact depth-dependent analysis of corneal elastic modulus, *Invest. Ophthalmol. Vis. Sci.* **54**, 1418–1425. https://doi.org/10.1167/iovs.12-11387.

30 Tao N.J., Lindsay S.M., Rupprecht A. (1988) Dynamic coupling between DNA and its primary hydration shell studied by Brillouin scattering, *Biopolymers* **27**, 1655–1671. https://doi.org/10.1002/bip.360271010.

31 Lee S.A., Lindsay S.M., Powell J.W., Weidlich T., Tao N.J., Lewen G.D., Rupprecht A. (1987) A Brillouin scattering study of the hydration of Li- and Na-DNA films, *Biopolymers* **26**, 1637–1665. https://doi.org/10.1002/bip.360261002.

32 Scarcelli G., Polacheck W.J., Nia H.T., Patel K., Grodzinsky A.J., Kamm R.D., Yun S.H. (2015) Noncontact three-dimensional mapping of intracellular hydromechanical properties by Brillouin microscopy, *Nat. Methods* **12**, 1132–1134. https://doi.org/10.1038/nmeth.3616.

33 Samalova M., Elsayad K., Melnikava A., Peaucelle A., Gahurova E., Gumulec J., Spyroglou I., Zemlyanskaya E.V., Ubogoeva E.V., Hejatko J. (2020) Expansin-controlled cell wall stiffness regulates root growth in Arabidopsis, *bioRxiv*, 2020.2006.2025.170969. https://doi.org/10.1093/plphys/kiad228.

34 Pethig R., Kell D.B. (1987) The passive electrical properties of biological systems: their significance in physiology, biophysics and biotechnology, *Phys. Med. Biol.* **32**, 933. https://doi.org/10.1088/0031-9155/32/8/001.

35 Carlton A., Orr R.M. (2015) The effects of fluid loss on physical performance: A critical review, *J. Sport Health Sci.* **4**, 357–363. https://doi.org/10.1016/j.jshs.2014.09.004.

36 Ross K.F.A., Gordon R.E. (1982) Water in malignant tissue, measured by cell refractometry and nuclear magnetic

resonance, *J. Microscopy* **128**, 7–21. https://doi.org/10.1111/j.1365-2818.1982.tb00433.x.

37  Lacevic N.M., Sader J.E. (2016) Viscoelasticity of glycerol at ultra-high frequencies investigated via molecular dynamics simulations, *J. Chem. Phys.* **144**. 054502. https://doi.org/10.1063/1.4940146.

38  Remer I., Shaashoua R., Shemesh N., Ben-Zvi A., Bilenca A. (2020) High-sensitivity and high-specificity biomechanical imaging by stimulated Brillouin scattering microscopy, *Nat. Methods* **17**, 913–916. https://doi.org/10.1038/s41592-020-0882-0.

39  Krug B., Koukourakis N., Czarske J.W. (2019) Impulsive stimulated Brillouin microscopy for non-contact, fast mechanical investigations of hydrogels, *Opt. Express* **27**, 26910–26923. https://doi.org/10.1364/OE.27.026910.

40  Elsayad K., Werner S., Gallemí M., Kong J., Sánchez Guajardo E.R., Zhang L., Jaillais Y., Greb T., Belkhadir Y. (2016) Mapping the subcellular mechanical properties of live cells in tissues with fluorescence emission-Brillouin imaging, *Sci. Signal* **9**, rs5. https://doi.org/10.1126/scisignal.aaf6326.

41  Meng Z., Traverso A.J., Yakovlev V.V. (2014) Background clean-up in Brillouin microspectroscopy of scattering medium, *Opt. Express* **22**, 5410–5415. https://doi.org/10.1364/OE.22.005410.

42  Edrei E., Gather M.C., Scarcelli G. (2017) Integration of spectral coronagraphy within VIPA-based spectrometers for high extinction Brillouin imaging, *Opt. Express* **25**, 6895–6903. https://doi.org/10.1364/OE.25.006895.

43  Khan R., Gul B., Khan S., Nisar H., Ahmad I. (2021) Refractive index of biological tissues: Review, measurement techniques, and applications, *Photodiagn. Photodyn. Ther.* **33**, 102192. https://doi.org/10.1016/j.pdpdt.2021.102192.

44  Annexes A.-D. (2009) Adult reference computational phantoms, *Ann. ICRP* **39**, 47–70. https://doi.org/10.1016/j.icrp.2009.07.005.

45  Bolin F.P., Preuss L.E., Taylor R.C., Ference R.J. (1989) Refractive index of some mammalian tissues using a fiber optic cladding method, *Appl. Opt.* **28**, 2297–2303. https://doi.org/10.1364/AO.28.002297.

46  Gelman S., Warner D.S., Warner M.A. (2008) Venous function and central venous pressure: A physiologic story, *Anesthesiology* **108**, 735–748. https://doi.org/10.1097/ALN.0b013e3181672607.

47  Ogneva I.V., Lebedev D.V., Shenkman B.S. (2010) Transversal stiffness and Young's modulus of single fibers from rat soleus muscle probed by atomic force microscopy, *Biophys. J.* **98**, 418–424. https://doi.org/10.1016/j.bpj.2009.10.028.

48  Camasão D.B., Mantovani D. (2021) The mechanical characterization of blood vessels and their substitutes in the continuous quest for physiological-relevant performances. A critical review, *Mater. Today Bio.* **10**, 100106. https://doi.org/10.1016/j.mtbio.2021.100106.

49  Troiani F., Nikolic K., Constandinou T.G. (2018) Simulating optical coherence tomography for observing nerve activity: A finite difference time domain bi-dimensional model,

*PLoS One* **13**, e0200392. https://doi.org/10.1371/journal.pone.0200392.

50  Lin M., Chen Y., Deng W., Liang H., Yu S., Zhang Z., Liu C. (2022) Quantifying the elasticity properties of the median nerve during the upper limb neurodynamic test 1, *Appl. Bionics. Biomech.* **2022**, 3300835. https://doi.org/10.1155/2022/3300835.

51  Sicard D., Fredenburgh L.E., Tschumperlin D.J. (2017) Measured pulmonary arterial tissue stiffness is highly sensitive to AFM indenter dimensions, *J. Mech. Behav. Biomed. Mater.* **74**, 118–127. https://doi.org/10.1016/j.jmbbm.2017.05.039.

52  Ryu S., Martino N., Kwok S.J.J., Bernstein L., Yun S.-H. (2021) Label-free histological imaging of tissues using Brillouin light scattering contrast, *Biomed. Opt. Express* **12**, 1437–1448. https://doi.org/10.1364/BOE.414474.

53  Timashev P.S., Kotova S.L., Belkova G.V., Gubar'kova E.V., Timofeeva L.B., Gladkova N.D., Solovieva A.B. (2016) Atomic force microscopy study of atherosclerosis progression in arterial walls, *Microsc. Microanal.* **22**, 311–325. https://doi.org/10.1017/s1431927616000039.

54  Margueritat J., Virgone-Carlotta A., Monnier S., Delanoë-Ayari H., Mertani H.C., Berthelot A., Martinet Q., Dagany X., Rivière C., Rieu J.P., Dehoux T. (2019) High-frequency mechanical properties of tumors measured by Brillouin light scattering, *Phys. Rev. Lett.* **122**, 018101. https://doi.org/10.1103/PhysRevLett.122.018101.

55  Landau L.D., Lifshitz E.M. (1987) in: Landau L.D., Lifshitz E.M. (eds), *Fluid Mechanics*, 2nd edn., Sound, Pergamon, pp. 263–324.

56  Holmes M.J., Parker N.G., Povey M.J.W. (2011) Temperature dependence of bulk viscosity in water using acoustic spectroscopy, *J. Phys.: Conf. Ser.* **269**, 012011. https://doi.org/10.1088/1742-6596/269/1/012011.

57  Antonacci G., Foreman M.R., Paterson C., Török P. (2013) Spectral broadening in Brillouin imaging, *Appl. Phys. Lett.* **103**, 012011. https://doi.org/10.1063/1.4836477.

58  Mattarelli M., Capponi G., Passeri A.A., Fioretto D., Caponi S. (2022) Disentanglement of multiple scattering contribution in Brillouin microscopy, *ACS Photon.* **9**, 2087–2091. https://doi.org/10.1021/acsphotonics.2c00322.

59  Ryu S., Martino N., Kwok S.J.J., Bernstein L., Yun S.H. (2021) Label-free histological imaging of tissues using Brillouin light scattering contrast, *Biomed. Opt. Express* **12**, 1437–1448. https://doi.org/10.1364/boe.414474.

60  Schlüßler R., Kim K., Nötzel M., Taubenberger A., Abuhattum S., Beck T., Müller P., Maharana S., Cojoc G., Girardo S., Hermann A. (2022) Correlative all-optical quantification of mass density and mechanics of sub-cellular compartments with fluorescence specificity, *eLife* **11**, e68490. https://doi.org/10.7554/eLife.68490.

61  Chan C.J., Bevilacqua C., Prevedel R. (2021) Mechanical mapping of mammalian follicle development using Brillouin microscopy, *Commun. Biol.* **4**, 1133. https://doi.org/10.1038/s42003-021-02662-5.